Title
Time resolved X-ray densitometry for cavitating and ventilated partial cavities

Journal
International Shipbuilding Progress, 60(1-4)

ISSN
0020-868X

Authors
Mäkiharju, SA
Perlin, M
Ceccio, SL

Publication Date
2013-08-20

DOI
10.3233/ISP-130086

Peer reviewed

Exp Fluids (2013) 54:1561
DOI 10.1007/s00348-013-1561-z

RESEARCH ARTICLE

Time-resolved two-dimensional X-ray densitometry of a two-phase flow downstream of a ventilated cavity

Simo A. Mäkiharju · Celine Gabillet · Bu-Geun Paik · Natasha A. Chang · Marc Perlin · Steven L. Ceccio

Received: 29 December 2012 / Revised: 29 May 2013 / Accepted: 31 May 2013

Abstract To measure the void fraction distribution in gas–liquid flows, a two-dimensional X-ray densitometry system was developed. This system is capable of acquiring a two-dimensional projection with a 225 cm^2 area of measurement through 21 cm of water. The images can be acquired at rates on the order of 1 kHz. Common sources of error in X-ray imaging, such as X-ray scatter, image distortion, veiling glare, and beam hardening, were considered and mitigated. The measured average void fraction was compared successfully to that of a phantom target and found to be within 1 %. To evaluate the performance of the new system, the flow in and downstream of a ventilated nominally two-dimensional partial cavity was investigated and compared to measurements from dual-tip fiber optical probes and high-speed video. The measurements were found to have satisfactory agreement for void fractions above 5 % of the selected void fraction measurement range.

Abbreviations

BFS	Backward-facing step
ESF	Edge spread function
FFT	Fast Fourier transform
II	Image intensifier
LSF	Line spread function
TTL	Transistor–transistor logic
PSF	Point spread function
RMSD	Root-mean-square deviation
SNR	Signal-to-noise ratio
2D	Two-dimensional

List of symbols

a_i	Fraction of light scatter contributed by term i
b_i	Measure of propagation distance of scattered light by term i
d	Bubble diameter (m)
D	The detected image
E	The un-degraded image
f_e	Bubble probe sampling frequency (1/s)
H	Height of the backward-facing step (127 mm)
$\widehat{H}$	Fourier transform of h
h	Point spread function ($1/m^2$)
I	Intensity of photon flux, number of photons per unit area and time ($1/(m^2 s)$)
G	Gray scale value of light intensity (1)
K	Number of X-ray image frames
L	Length (m)
l_{12}	Streamwise distance between the optical probe's tips (m)
l_L	Latency length of the optical probe's tips (m)
l_c	Chord length of the gas measured by the upstream tip of the optical probe (m)
N	Total number of materials (1)
n_b	Number of gas structures detected on the upstream tip of optical probe
Q	Injected air volume flow rate (m^3/s)
Q_{det}	Image intensifier detection efficiency

S. A. Mäkiharju (✉) · M. Perlin · S. L. Ceccio
University of Michigan, Ann Arbor, MI, USA
e-mail: smakihar@umich.edu

C. Gabillet
Research Institute of the French Naval Academy, École Navale, Brest, France

B.-G. Paik
Korea Institute of Ocean Science and Technology, Daejeon, Korea

N. A. Chang
Naval Surface Warfare Center, Carderock Division, Bethesda, MD, USA

Published online: 20 June 2013

q Non-dimensional gas flow rate, Q/UHW (1)
r Radial distance (m)
Re Reynolds number, UL/v (1)
t Time (s)
t_a Transit time of a gas structure between the two tips of the optical probe(s)
t_{aP} Most probable transit time of gas structures (s)
T Measurement time of the bubble probe (s)
U Free-stream velocity at the BFS (m/s)
U_a Gas velocity (m/s)
$\overline{U}_a$ Statistical mean value of the gas velocity (m/s)
U_{aP} Most probable velocity of the gas (m/s)
U_w Water velocity (m/s)
W Width of the model (209.6 mm)
v Bubble probe signal voltage (V)
V Photon energy (eV)
x_n Mass thickness of material, n (kg/m^2)
x Coordinate along the test surface, zero at the BFS (m)
y Coordinate normal to the test surface (m)
z Spanwise coordinate (m)

Greek letters

α Void fraction (1)
δ Boundary layer thickness (m)
Δ Linear dimension of a square on imager
ε_α Error in void fraction (1)
ρ Density (kg/m^3)
θ Momentum thickness (m)
σ Surface tension (N/m)
v Kinematic viscosity (m^2/s)
μ_n/ρ_n Mass attenuation coefficient of material n (m^2/kg)

Subscripts

a Air
i, j Number of term
inj Injection
k Frame number
m Mixture
min Minimum
max Maximum
n Material designator (air, water, mix, etc.)
OP Optical probe
w Water
0 Initial
2 Two-dimensional

1 Introduction

Gas–liquid and cavitating flows are encountered in many industrial and hydrodynamic applications, and it is often of considerable interest to understand the evolution and dynamics of the local volume fraction of gas or vapor. This is particularly important as we seek to develop physics-based models of multiphase flows to predict the spatial and temporal evolution of the void fraction field. However, measurement of the local time-dependent void fraction has not always been possible, especially in higher speed flows where probes inserted into the bulk of the flow may perturb the flow considerably or where the flows are optically opaque. Hence, it is desirable to develop measurement techniques that reveal the spatial distribution of the phase fractions without disturbing the flow.

In many applications, to measure the void fraction in a cavitating or other multiphase flow in a non-intrusive manner, electrical resistance and impedance techniques have been used quite successfully (Van Der Welle 1985; Ceccio and George 1996; George et al. 2000a, b; York 2001; Holder 2005; Elbing et al. 2008). Impedance probes have been developed that are installed from flush to a flow boundary or are inserted into the flow; also, multiple boundary measurements of impedance can be used to deduce the impedance distribution within a domain (Cho et al. 2005). Combined with a model that relates the fluid phase topology (e.g., bubble, stratified) and the local impedance, the impedance field can be used to find the phase distribution. Impedance tomography systems have been developed successfully for gas–liquid, gas–solid, and three-phase flows, and a recent review is provided by Holder (2005). Impedance tomography systems can be constructed at relatively low cost and can be designed to provide temporally resolved phase fields. The spatial resolution of such systems is limited by the finite size and hence number of electrodes that can be located on the domain boundary. And, most importantly for gas–liquid flows, the reconstruction of the impedance field is based on a "soft-field," where the result is dependent on the flow topology, and oftentimes, an a priori knowledge of the phase distribution may be required to obtain a solution.

Conversely, radiation densitometry and tomography have the benefit of being a hard-field measurement, such that the beam path is not dependent on the distribution of the phases within the domain. Both gamma and X-ray sources have been used to examine multiphase flows, and several researchers have used X-ray imaging to investigate both cavitating flows (Stutz and Legoupil 2003; Coutier-Delgosha et al. 2007; Hassan et al. 2008; Aeschlimann et al. 2011) and bubbling fluidized beds (Hubers et al. 2005). A recent article by Heindel (2011) provides a comprehensive review of the use of X-ray systems in multiphase flow.

Presented here are the details of an X-ray densitometry system that has been developed to measure the volume fraction fields of nominally two-dimensional flows without the need for phase averaging. Our goal was to develop a system that would be appropriate for relatively high

Reynolds number gas–liquid flows at laboratory scale, with length of the flow domain on the order of 0.2 m, and speeds to 10 m/s. For water flows, this would yield a Reynolds number on the order of 2 million. To resolve the dynamics of such a flow, the X-ray densitometry system would need to measure the phase fields at a minimum rate of 1,000 frames per second.

As we intend to use the X-ray densitometry system to provide validation–quality data, we have attempted to characterize the most important sources of uncertainty associated with the measurement and to account for their effect when possible. We then performed X-ray measurements on a two-dimensional cavity flow and compared these measurements to those performed with optical probes and videography to further understand the advantages and limits of the densitometry system.

The manuscript is organized in the following manner. In Sect. 2, we summarize the basic X-ray densitometry technique and discuss some of its limitations and sources of uncertainty in our measurement of void fraction. In Sect. 3, we briefly discuss the optical probe measurement technique. In Sect. 4, we describe the partial cavity flow and the other associated measurement techniques. In Sect. 5, the measurements from the X-ray densitometry system are compared and contrasted with those from the bubble probes and high-speed videography. The conclusions are provided in Sect. 6.

2 The X-ray imaging system

2.1 Physical principles

When a beam of high-energy X-ray photons encounters an object, a fraction of the photons passes through without scattering or absorption (attenuation). The fraction of attenuated photons depends on the object's mass attenuation coefficient, density, and thickness. For a beam encountering a domain with N distinct materials, based on the Beer–Lambert law, we can write

$$\frac{I}{I_0} = \mathrm{e}^{-\sum_{n=1}^{N} x_n \mu_n/\rho_n} \tag{1}$$

where I_0 is the original intensity of the photon beam at any given energy, I is the intensity of the transmitted beam, μ_n/ρ_n is the mass attenuation coefficient, ρ_n is the density, x_n is the mass thickness ($x_n = \rho_n t_n$), and t_n is the thickness over the traversed beam path through material n. The attenuation coefficient is a function of material properties and photon energy, and is a known property for most common materials (Hubbell and Seltzer 2004). Based on Eq. 1, we can derive an equation relating the attenuation to the void fraction of a two-phase mixture (Stutz and Legoupil 2003; Hubers et al. 2005). A step-by-step derivation with the assumptions highlighted was provided also in Mäkiharju (2012). The void fraction, α, of a two-phase mixture of air and water along any given beam path can be written as

$$\alpha = \ln\left(\frac{I_m}{I_w}\right) \Big/ \ln\left(\frac{I_a}{I_w}\right) \tag{2}$$

where I signifies the intensities of photon fluxes that pass through a test section filled with a mixture, m, all water, w, or all air, a, at any one given photon energy, V. This relationship is valid for a monochromatic beam. But, as we shall discuss below, the X-ray source used is polychromatic, and hence, use of Eq. 2 without full knowledge of $I_n = I_n(V)$ introduces additional uncertainty.

2.2 Description of the X-ray imaging setup

The components of the X-ray densitometry system are shown in Fig. 1. The operator sets the X-ray tube's current, voltage, duration of exposure, and selects the image intensifier's field size and attendant camera settings. Once an exposure is initiated, a signal is sent to the trigger unit (Stanford Research Systems model DG535 delay generator), which after a specified delay sends a TTL signal to the high-speed camera. Figure 2 shows the arrangement of the source, test section, and imager, as well as the X-ray cone beam.

The X-ray photon flux needs to be sufficiently high, both in the number and energy of photons, to insure that a significant fraction passes through the domain. On the other hand, the energy must be low enough that sufficient attenuation occurs over short distances to yield an adequate contrast and signal-to-noise ratio when there are subtle differences in void fraction. Also, it was desired that the

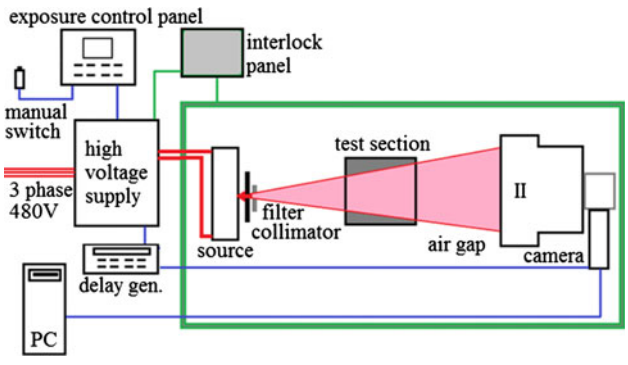

Fig. 1 A schematic diagram showing the key components of the X-ray densitometry system. The *green rectangle* represents the interlocked shielding. The shielding was originally designed for a higher energy source, and therefore, the walls directly intersecting the beam had an excessive lead thickness of 25 mm. Walls potentially grazed by the beam at *shallow angles* or exposed only to scattered radiation had lead thicknesses of 19 and 13 mm, respectively

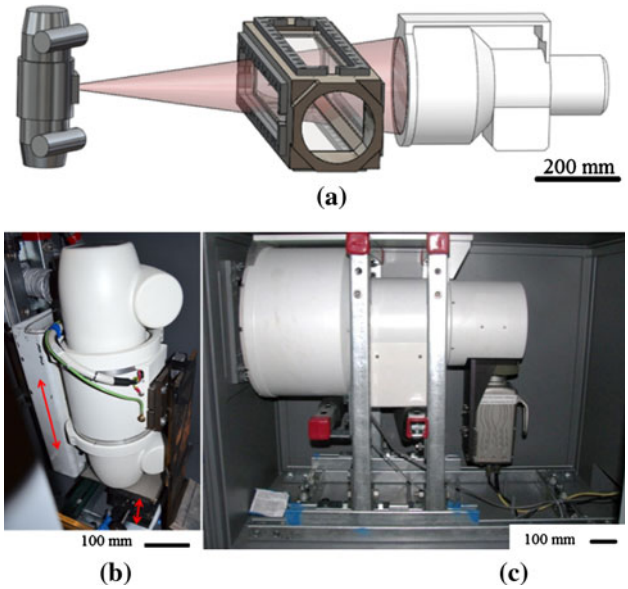

Fig. 2 The basic arrangement and components of the X-ray densitometry system. **a** Schematic of the system with the source on the *left*, test section in the *middle*, and image intensifier on the *right*. The *red cone* indicates the path of the X-ray beam. **b** The X-ray source mounted on a repositionable frame. **c** The image intensifier with the high-speed optical camera

photon energy levels be suitable for use with commercial image intensifiers (II). The source selected is comprised of a Varian G-1092 insert in a Varian B-160H housing (Fig. 2b). This is a regular 150 kV rotating anode tube designed for radiography, cineradiography, and angiography. It can be operated to 800 mA (at 81 kV) or 433 mA (at 150 kV), when supplied by the chosen 65 kW high-frequency (100 kHz) generator with a high-speed starter (CMP 200 DR). The source had a selectable focal spot size of 0.6 or 1.2 mm, allowing less focal spot blur or higher power when using the smaller or larger spot size, respectively. The cone beam originating from the focal spot has a 24° included angle.

The imager subsystem (Fig. 2c) is comprised of a high-speed camera (Vision Research v9.0) coupled with a high efficiency, high-resolution II. A tri-field (30.5/22.9/15.2 cm diameter) II was chosen to enable image magnification without altering the physical setup of the experiment. For the current experiments, the 22.9 cm input area was utilized. This II has a resolution of 48/54/62 line pairs per centimeter, conversion factor of 320 $\mathrm{cdm^2/mRs^{-1}}$, and 65 % detective quantum efficiency at 59 keV. An ordinary image intensifier was chosen, rather than an array of detectors, as an economical system that is still capable of rapidly acquiring information of the attenuation through multiple beam paths (i.e., to acquire an instantaneous two-dimensional projection without phase averaging). After passing through the flow domain, the incoming X-ray photons enter the imager enclosure through a view-port and interact with the II's input phosphor to produce photons in the visible wave lengths that are then converted into electrons. These electrons are accelerated and incident on a second output phosphor. The output phosphor produces photons in the visible wavelengths detectable by an ordinary high-speed camera. The light collected at each of the camera's 1.92 million pixels (or a subassembly of neighboring pixels) gives a measure of attenuation through one unique beam path. In the following subsection, we will discuss the characteristic of the systems, the most important sources of uncertainty, and the steps that can be taken to ameliorate them.

2.3 X-ray scatter

X-ray photons are scattered from matter in the beam's path, and this can obscure the image details. To minimize this effect in medical applications, use is made of anti-scatter grids, and in some cases air gaps. In the current experiments, a collimator at the source and an air gap between the object and imager were used. The principle is to minimize the number of scattered X-rays reaching the imager; an air gap helps because the scattered photons tend to have large angles, different from those of the primary beam's photons. The collimator is used to narrow the cone beam at the source, so that only the part of the beam illuminating the area of interest enters the domain.

2.4 Effect of beam hardening on the measured void fraction

Except for monochromatic sources, an X-ray beam contains photons across a continuous spectrum of energies. Many detectors, including those used in the current research, do not resolve photon energy. The fraction of the beam that makes it through a domain varies with photon energy. As shown in Fig. 3a, the lower energy photons in the spectrum are attenuated preferentially compared to the higher energy photons (Hubbell and Seltzer 2004), leading to an increase in the average photon energy within the beam, denoted as beam hardening. Also, when using a polychromatic source and non-energy resolving detector, the value actually measured by the detector is the gray scale value of the detected light intensity, G, and not I, as defined in Eq. 2. The light intensity at each pixel of the camera is related to intensity I by

$$G \propto \left(\int_0^{V_{\max}} I(V) Q_{\det}(V) V dV \right) \tag{3}$$

where V is the photon energy, $I(V)$ is number of photons of energy V incident on a given area of the imager screen, and

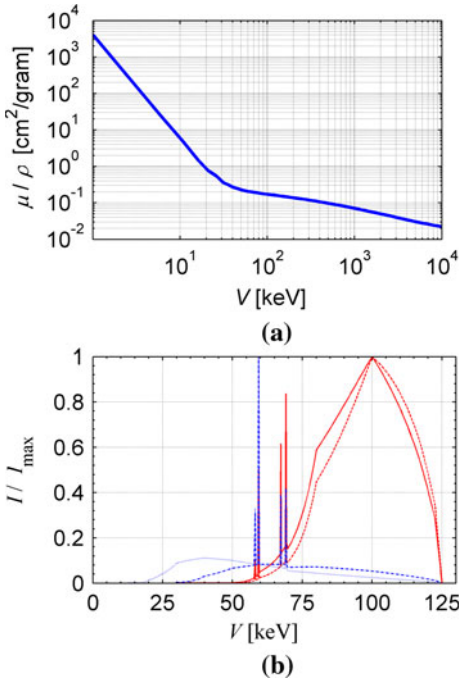

Fig. 3 **a** The mass attenuation coefficient, μ/ρ, of water as a function of photon energy, V (Hubbell and Seltzer 2004). **b** The effect of beam pre-hardening on the incident and transmitted photon energy spectra. Presented as the normalized beam spectrum versus photon energy, V, after passing through the 109.6 mm wide test section and 38 mm of acrylic. The *dotted* and *dot-dashed blue curves* show the normalized spectra for 0 and 100 % void fractions without pre-hardening, respectively. With pre-hardening using a 6.4 mm thick steel plate, the *solid* and *dashed red curves* show the normalized spectra for 0 and 100 % void fractions, respectively. The X-ray source spectrum was simulated using SpecCalc by Poludniowski et al. (2009)

$Q_{\text{det}}(V)$ is the image intensifier's detection efficiency (the efficiency at which X-ray photons are transformed into photoelectrons and then into photons in the visible range). As both the attenuation and detection efficiency depend on the energy of the X-ray photons, V, I/I_0 and G/G_0 are not equivalent and this can lead to an error in the measured void fraction, as we shall see next.

A polychromatic beam passing through material will always be hardened, and the low energy portion of the beam practically disappears, while a large fraction of the higher energy photons passes through the material. As will be shown in this section, it can be beneficial to always attenuate most of the lower energy photons, even when the domain has a high void fraction. We do this by "pre-hardening" the polychromatic beam by placing a filter between the source and object that we are imaging. For these experiments, the beam was pre-hardened by a filter, which consisted of an ordinary carbon steel plate. To estimate the effect of beam hardening, the attenuation of the beams passing through the test section and two-phase domain was simulated. The X-ray source's spectrum was estimated using the SpecCalc-software by Poludniowski et al. (2009). Figure 3b shows the simulated normalized photon energy spectra before and after the domain for cases with and without pre-hardening. Note that, beam hardening modifies the shape of the spectrum of an X-ray beam as it passes through a domain, and lower energy photons in the spectrum are attenuated preferentially. However, the pre-hardened beam has a similar shape regardless of the void fraction. Consequently, the error arising from use of Eq. 2 with a polychromatic beam is modified, and the results are presented in Fig. 4. The error is dependent on the void fraction in the domain, but for all void fractions, it can be seen that for the case simulated, pre-hardening reduces the potential error significantly. For example, at 50 % void fraction, the error with and without pre-hardening is 0.24 and 2.77 %, respectively.

Alles and Mudde (2007) discuss the effects of beam hardening further and introduce "effective attenuation coefficients" for tomography. However, as shown in Fig. 4, for the cases discussed in this paper, the maximum bias error due to beam hardening can be reduced to less than 0.5 % by simply pre-hardening. Thus, this value is small compared to other sources of error and uncertainty discussed in the following sections. And, as the energy spectra were not measured to allow for empirical correction, pre-hardening alone was used to mitigate the effects of beam hardening in the current set of experiments.

2.5 Estimating uncertainty of the measured void fraction

To estimate uncertainty in the measured void fraction, we first considered that an 8-bit camera was utilized in the current setup. Therefore, absence of light corresponds to a gray scale value, G, of zero while the sensor saturates at a value of 255. To ensure that the sensor was never saturated, and that some light was reaching it, we chose the source settings with the aim of having the values of G at minimum

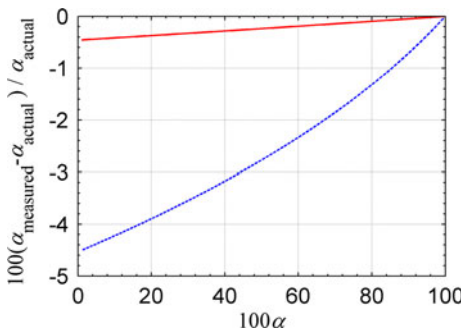

Fig. 4 The relative percent error in the measured void fraction versus the actual void fraction determined with Eq. 2, with a polychromatic beam and direct substitution of the detected light intensity, G, for number of photons at given energy, $I(V)$. The *solid* and *dashed lines* are for with and without pre-hardening, respectively

and maximum void fractions be $G \sim 10$ and ~ 245, respectively. The actual values achieved were 6 and 240 for the example we will discuss. To obtain a reasonable estimate of the accuracy of the void fraction measurement (for a single pixel in a single frame), we assumed that each pixel of the camera was correct to within $\pm\Delta G$, where ΔG is the uncertainty in the intensity. Assuming that each variable of Eq. 2 is uncorrelated, the overall error in the resulting void fraction can be estimated as

$$\varepsilon_\alpha = \sqrt{\left(\Delta G_\mathrm{m}\frac{\partial\alpha}{\partial G_\mathrm{m}}\right)^2+\left(\Delta G_\mathrm{a}\frac{\partial\alpha}{\partial G_\mathrm{a}}\right)^2+\left(\Delta G_\mathrm{w}\frac{\partial\alpha}{\partial G_\mathrm{w}}\right)^2}. \tag{4}$$

here, the void fraction, α, is based on Eq. 2. Assuming further that the uncertainty of intensity when measuring mixture, air, or water is the same ($\Delta G_\mathrm{m} = \Delta G_\mathrm{a} = \Delta G_\mathrm{w}$) we can write

$$\varepsilon_\alpha = \frac{\Delta G_\mathrm{m}}{G_\mathrm{a}G_\mathrm{m}G_\mathrm{w}\ln^2\frac{G_\mathrm{a}}{G_\mathrm{w}}} \times \sqrt{G_\mathrm{a}^2\left(G_\mathrm{m}^2+G_\mathrm{w}^2\right)\ln^2\frac{G_\mathrm{a}}{G_\mathrm{w}} - 2G_\mathrm{a}^2G_\mathrm{m}^2\ln\frac{G_\mathrm{a}}{G_\mathrm{w}}\ln\frac{G_\mathrm{m}}{G_\mathrm{w}} + G_\mathrm{m}^2\left(G_\mathrm{a}^2+G_\mathrm{w}^2\right)\ln^2\frac{G_\mathrm{m}}{G_\mathrm{w}}}. \tag{5}$$

For the case of $\Delta G = \pm 1$, for example, intensity with zero void fraction $G_\mathrm{w} = 6$ and with void fraction of unity $G_\mathrm{a} = 240$, we find the results presented in Fig. 5. This demonstrates that the error due to an incorrect gray scale value would increase exponentially as we go toward the low void fractions (corresponding to low G). That is, in both relative and absolute terms, the uncertainty is larger at lower void fractions.

The noise of the source, II, and camera affects the spatial, temporal, and void fraction resolutions. Presumably, the noise is Gaussian and has zero bias, and therefore, with a sufficiently large data sample, the effect of noise would be mitigated after averaging. However, with short sample times, especially when imaging at 1 kHz, each of the camera's pixels received light generated by a relatively small number of X-ray photons, making the random noise of the source also potentially significant. The signal-to-noise ratio (SNR) can be defined for each pixel as the ratio of its mean value and root-mean-square deviation (RMSD). And $RMSD = \sqrt{\frac{1}{K}\sum_{k=1}^{K}\left(G_k-\overline{G}\right)^2}$, where K is the number of frames (typically ~ 700) and G is the intensity at the pixel of interest. This SNR can vary depending on the flow condition, exposure, and camera

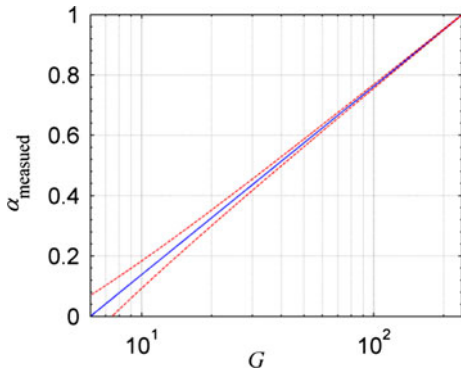

Fig. 5 The measured void fraction (*solid blue line*) and uncertainty envelope (*dashed red lines*), as a function of the *grey* scale value, G, for $\Delta G = \pm 1$, $G_w = 6$, and $G_a = 240$

settings. In the region of interest in the ventilated cavity experiments, for an image of the empty test section, the SNR was found to range from 22 to 62, with a 29 mean. A more comprehensive discussion of II noise is given by Bushberg et al. (2001).

The source intensity also had a slow drift, $O(1\ \%)$. According to the source's manufacturer (Varian), the flux of photons from the X-ray source has time dependence caused by the generator, filament heating, anode heating, etc. For each set of images, the mean image intensity was plotted as a function of frame number. For all the void fraction calculations, data were considered only after the mean intensity was within $\sim 0.5G$ of the final value. (If the recording was started before the intensity was within $\sim 0.5G$ of its final value, or extended beyond the exposure time, the dataset was cropped accordingly.) Based on Eq. 5, the error caused by a $0.5G$ drift can be estimated as 2.6 and 0.2 % at 10 and 90 % void fractions, respectively.

Thereafter, a direct validation and accuracy quantification of the void fraction measurement were conducted by placing a domain of known volume fraction in the beam path. Six containers with parallel walls spaced 1.6–101.6 mm apart were constructed as void fraction calibration "phantoms." The baseline attenuation due to the test section and container material cancels, as can be seen, when deriving Eq. 2. The combined path thickness of water was varied from 0 to 191.3 mm. The cumulative

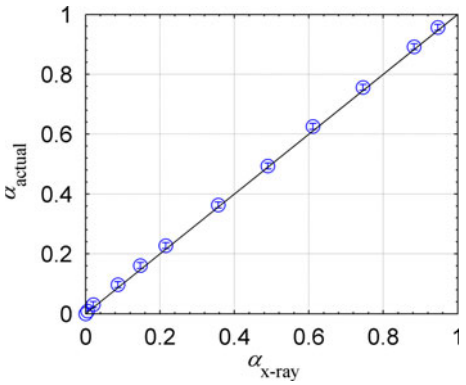

Fig. 6 The actual void fraction based on the container thicknesses and water content versus the void fraction measured via X-ray. The *circles* are measured results, and the *solid line* is the ideal *curve*. Measured void fraction was based on an average of 200 frames and an area of 60,000 pixels

uncertainty of the water path length through the six calibration volumes was estimated to be 1–2 mm, leading to a 0.5–1.0 % uncertainty in the reference void fraction. Figure 6 shows the results from 14 different fill combinations with void fraction ranging from 0 to 1. The highest deviation, 0.0074, demonstrates the accuracy of the average void fraction measurement and is comprised likely of bias error due to container thickness; random variation of the source strength, I_0; bias error varying with void fraction due to beam hardening; and the varying effect of ΔG as a function of the void fraction.

2.6 The limiting spatial resolution

The resolution of the camera itself limits the highest detectable spatial frequency. Based on the Nyquist criterion, the highest distinguishable spatial cyclic frequency, $f_{max} = 1/2\Delta$. In our case, Δ is the linear dimension of a square area on the II's input plane, which is mapped onto a single pixel on the camera's CMOS. The Vision Research Phantom V9.0 camera used has a 1,632 by 1,200 pixel CMOS. For the lenses used in the system, the image of the output phosphor is mapped onto a circle of diameter 1,360 pixels. For the 305/229/152 mm (12/9/6 inch) selectable input sizes $\Delta = 0.22/0.17/0.11$ mm. Therefore, the camera alone limits the highest spatial frequency to 2.2, 3.0, and 4.5 mm^{-1} for the 305, 229, and 152 mm input fields, respectively.

The spatial resolution of the entire system was quantified experimentally by two methods. First, a standard resolution test tool, with 0.63–1.97 lines/mm grids, was used. The test tool was placed near the flow domain. The results indicated that in the basic system configuration, we can resolve approximately 1.6 lines/mm. Secondly, the resolution was quantified based on the line spread function (LSF) full width at half of its maximum value. (The LSF is the in-plane derivative of the detected intensity variation normal to the image of a sharp edge [i.e., the derivative of the edge spread function (ESF).] According to this definition, based on the data presented in Fig. 7, the spatial resolution is determined to be 0.46 mm. As expected (as the resolution is limited also by veiling glare, blur due to finite focal spot size and X-ray scatter), this is slightly larger than the resolution limit imposed by the camera alone, which was 0.33 mm.

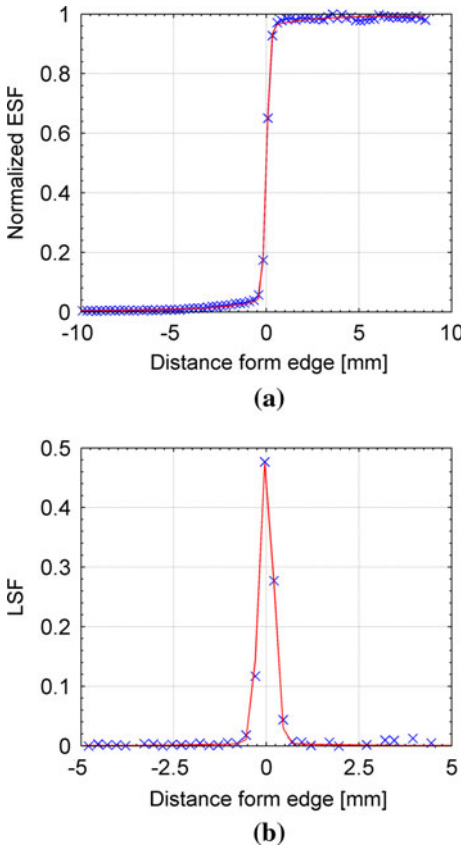

Fig. 7 **a** The imaging system edge spread function (*ESF*). The *symbols* are measured data obtained by placing a 1.6 mm thick lead plate directly onto the II input screen and plotting the normalized intensity variation normal to the plate edge. The *solid line* is a least squares fit to Eq. 10, which yields coefficients $a_1 = 0.08811$, $a_2 = 0.91189$, $b_1 = 1.722$ mm and $b_2 = 0.244$ mm; **b** Data *points* and *line* showing the line spread function (*LSF*) of the measured data and the LSF corresponding to ESF fit shown in **a**. The full width of the LSF at half of its maximum value corresponds to 0.46 mm in the object plane

2.7 Correction for image distortion

The X-ray image of any two-dimensional object placed in the cone beam's path is distorted because the paths of the X-rays are not parallel over the domain (except possibly for a single beam path at a particular angle), and the image intensifier introduces distortion due to its geometry and the imperfections of its electric fields (Bushberg et al. 2001).

Additionally, the camera optics can also distort the image of the II's output phosphor.

Correction for non-parallel beam path distortions was not feasible due to the noise in the signal and having only a single projection, i.e., having no redundant data (Mäkiharju 2012). Correcting for the remaining types of distortion is straightforward. Numerous researchers have proposed unwarping algorithms to correct for these distortions. For instance, Cerveri et al. (2002) discuss local unwarping polynomials and radial basis function neural networks. For our part, we used a calibration image and followed a procedure similar to that used in particle imaging velocimetry, except that the calibration grid was placed on the imager directly, and the markers had different attenuation than the surrounding material. We found that the dewarping functions in LaVision's DaVis 7.2 provided an acceptable correction in the form of two-dimensional 3rd-order polynomials. Once found, the polynomials were implemented in a Matlab code and used to dewarp all the images. Figure 8 shows an aluminum calibration grid that was placed on the II-screen, as well as the unmodified and dewarped X-ray image of the calibration target. As is evident in Fig. 8c, the distortion correction was successful.

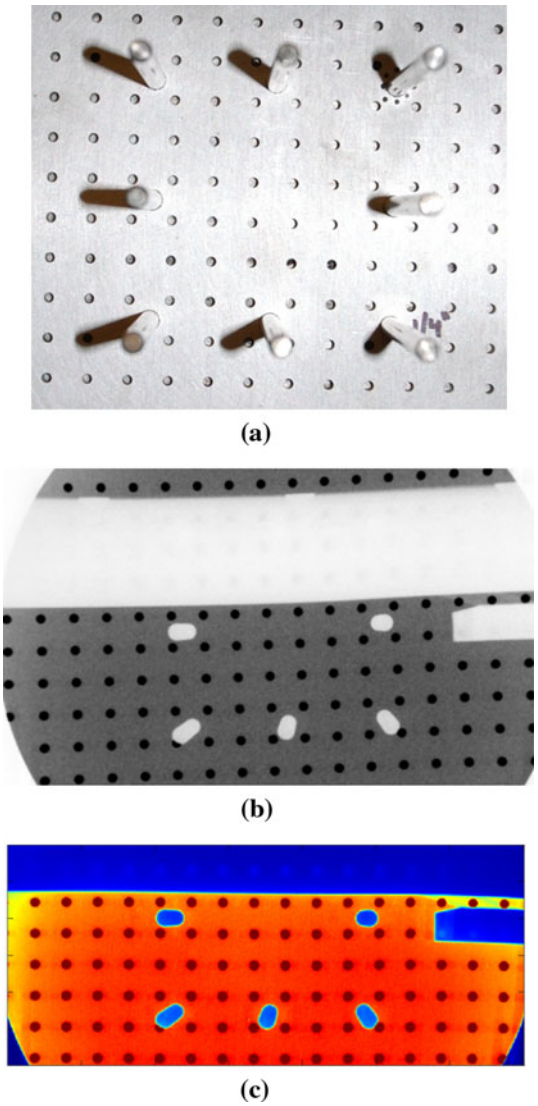

Fig. 8 **a** Photograph of the aluminum plate used as a calibration target with 3.3-mm holes that are spaced regularly at 12.7 mm. Projections from the 150 mm *long parallel rods* were employed to determine the relative location of the source and imager; **b** negative X-ray image of the bottom part of the calibration plate before distortion correction (with the model partially obscuring the plate); **c** a portion of image **b** shown after distortion correction. The *colors* correspond to different *grey* scale values

2.8 Correction for veiling glare

Veiling glare tends to smooth sharp interfaces between different volume fractions, and it is particularly obvious and detrimental to image quality, when high intensity and low-intensity regions are nearby in the same image. This occurs in regions of strong void fraction gradient, such as free surfaces. Veiling glare is related to photon scatter within the imager system. Significant scattering can occur in the II's output phosphor (Seibert et al. 1984), although the scattering of photons and electrons in the input screens, and the scattering of visible wavelength photons in the camera's lenses can also contribute.

The image recorded by the camera can be treated as a convolution of the un-degraded image with the point spread function (PSF) of the imager. Thus, correction for veiling glare can be attempted using deconvolution as in Seibert et al. (1984, 1985) and Seibert and Boone (1988), and we can write

$$D = h * *E \tag{6}$$

where D is the detected image, h is the PSF, ** signifies a 2D convolution, and E is the un-degraded image we wish to recover. In the frequency domain, this can be written as a multiplication

$$F_2[D] = F_2[h]F_2[E]. \tag{7}$$

Here, F_2[A] denotes the two-dimensional Fourier transform of any variable A. We solve for E by dividing through by the Fourier transform of h and performing the inverse Fourier transform F_2^{-1}, yielding

$$E = F_2^{-1}\left[F_2[D]\frac{1}{F_2[h]}\right] = F_2^{-1}\left[F_2[D]\widehat{H}^{-1}\right] \tag{8}$$

Seibert et al. (1985) proceed by analytically transforming h to obtain its Fourier transform's reciprocal, $\widehat{H}^{-1}$. Alternatively, we can employ a known or assumed PSF with common deconvolution algorithms. In the present work, we

employed Matlab's built-in function, "deconvlucy," based on the Lucy–Richardson method.

To correct the image, several possible point spread functions are discussed by numerous authors including Seibert et al. (1984), Smith (2006), and Poludniowski et al. (2011). The last reference provides a very general form of PSF, from which most proposed PSFs can be extracted:

$$h(r) = (1 - a_1 - a_2 - a_3)\frac{\delta(r)}{2\pi r} + \frac{a_1}{2\pi b_1^2} e^{-\frac{1}{2}\left(\frac{r}{b_1}\right)^2} + \frac{a_2}{2\pi b_2^2} e^{-r/b_2} + \frac{a_3}{2\pi b_3^2} \frac{1}{\left(1 + r^2/b_3^2\right)^{3/2}}. \quad (9)$$

here, a_1, a_2, and a_3 are coefficients that can be thought to be related to the fraction of light scattered by various processes (represented by the different terms), r is the radial distance, b's can be considered to relate to mean propagation distances of scattered light, and δ (r) is the Dirac delta function of r.

The ESF is straightforward to measure, and for that reason, it was used to estimate the PSF. For the current data, we used the relationships between ESF and PSF given in Johnson (1973). Therefore, the ESF given by

$$\mathrm{ESF}(x) = a_1\left[\frac{1}{2} + \frac{1}{\pi}\tan^{-1}\left(\frac{x}{b_1}\right)\right] + a_2\left[\frac{1}{2} + \frac{1}{2}erf\left(\frac{x}{b_2}\right)\right] \quad (10)$$

where x here is the coordinate normal to the edge, is related to the point spread function

$$h(r) = (1 - a_1 - a_2)\frac{\delta(r)}{2\pi r} + \frac{a_1}{2\pi b_1^2} \frac{1}{\left(1 + r^2/b_1^2\right)^{3/2}} + \frac{a_2}{4\pi b_2^2} e^{-\frac{1}{4}\left(\frac{r}{b_2}\right)^2}. \quad (11)$$

Again, a_1 and a_2 are coefficients that relate the fraction of light scattered by various processes. However, we will simply treat these as empirical fit parameters. As seen in Fig. 7a, a least squares approximation of Eq. 10 matched the data well with coefficients $a_1 = 0.08811$, $a_2 = 0.91189$, $b_1 = 1.722$ mm, and $b_2 = 0.244$ mm. With these coefficients, Eq. 11 was used to correct for the veiling glare in the cavity closure region. To avoid high-frequency oscillations, the term with the lower value of b was set to zero for the deconvolution, as done by Poludniowski et al. (2011). The effect of this correction is seen in Fig. 12d.

2.9 The limiting temporal resolution

The temporal resolution of the X-ray-based void fraction measurements is limited by the camera's frame rate, number of photons available to record data with sufficiently high SNR and by the imaging system's response time. The imaging system's response time is set by the finite rise and decay times of the II's phosphor. The data sheet for a nominally identical image intensifier (Thales 2006) lists that for a 5 mR/s exposure, the luminescence rises to 50 and 80 % of the final value in 1 and 10 ms, respectively. The reported decay times are 1 and 10 ms to decay to 30 and 10 %, respectively. Thus, the decay rate will not conform to a single time constant, τ, fitting $e^{-t/\tau}$. However, based on the 10 ms luminosities alone, the rise and decay time constants would be 6.2 and 4.3 ms, respectively.

We attempted to quantify the imager's response time by two methods. First, the response time was based on the measured variation of light intensity at the beginning and end of exposure, and assuming the source's rise and decay times to be orders of magnitude faster (so that any lag in the rise of intensity would be due to the phosphor). This approach suggested that the imager's time constant would be $\tau \approx 4.3$ ms. The second approach was to place a metallic disk spinning at 386 rpm in front of the source. The disk had a 6.4 mm hole located 28.1 mm from the center of rotation. By recording an X-ray movie at 1,000 fps of the spinning disk and plotting the time trace of mean intensity over a 10-by-10 pixel region, it was found that the intensity at a given location reaches 32, 63, and 90 % of the final value within 1, 2, and 9 ms, respectively.

While the phosphor's decay time constant is O(3 ms), differences over shorter time periods are clearly detectable, and for similar imagers O(10 kHz), frame rates have been used successfully (e.g., Aeschlimann et al. 2011). Therefore, for the current experiments, where data were acquired to 1 kHz, it is postulated that changes over 1 ms time scales can be reliably detected and the information used, as long as the limitations of the system are understood. In the current work, our highest flow speed was 1.8 m/s, and hence, a bubble could move 1.8 mm in the 1 ms interval between frames. While some ghosting was certainly present, it was not readily observable in the data.

2.10 The X-ray image processing procedure

To process the data while satisfying the previously discussed criteria and optionally accounting for veiling glare, when its effect was significant, the following procedure was adopted. First, each movie was processed to produce a time trace of frame-averaged image intensity, which then was used to register when the recording was initiated compared to the time that the source was energized. Then, a range of frames was defined wherein the average image intensity was nominally constant. Within this range, all frames were averaged to obtain the average intensity for each pixel for the all air G_a, all water G_w, and mixture G_m

conditions. Second, each image was corrected for geometric distortions and the data were mapped onto a new image where, depending on the spatial averaging chosen, each new larger pixel had an average intensity based on that of 4 to 100 of the original pixels. Third, and the optional step, a veiling glare correction was applied via Lucy–Richardson deconvolution with 10 iterations. Fourth, the void fraction at each pixel of each frame was calculated based on Eq. 2, with the physical constraints limiting the results such that $\alpha(t, x, y) = 0$ if $G_{\mathrm{m}}(t, x, y) < G_w$ and $\alpha(t, x, y) = 1$ if $G_{\mathrm{m}}(t, x, y) > G_{\mathrm{a}}$, which occasionally occurred due to statistical variation and light scatter. These corrected images were deemed the X-ray results.

3 Optical bubble probes

A dual-fiber optical probe and an optoelectronic module made by RBI-Instrumentation were used to measure the void fraction, streamwise gas velocity, U_a, and bubble size distributions. The optoelectronic module was used to inject light into the fibers of the probe, detect the reflected signals, and convert them into voltage levels. The end of each optical fiber had a cone-shaped tip. Owing to the different refractive indices, the amount of light reflected back to the optoelectronic module will vary depending on whether the tip is immersed in a gas or a liquid. The probe consisted of two 30 micron sapphire tips, separated in the streamwise direction by distance l_{12} that was 1.05 mm (Fig. 9).

To reliably detect a gas structure pierced by the tip, the gas residence time on the tip must be larger than the response time of the dewetting–rewetting process. Then, the resolution of the tips is limited by the response time of the tips during the dewetting process (response time of the rewetting process being much shorter). As shown in Cartelier (1990), above a critical velocity, around 0.2 m/s, the response time of the dewetting process is expected to evolve as the inverse ratio of the gas interface velocity. Thus, the product between the response time of dewetting and the interface velocity (i.e., the latency length) remains constant. The latency length is representative of the size of the smallest gas structure that can be detected by the probe's tips with a good accuracy. The latency length l_L has

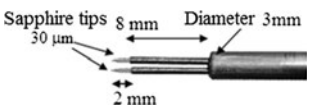

Fig. 9 The dual-fiber optical probe used in the comparison experiments. The tips of the probe are made of sapphire and are 2 mm long and with a 30 micron diameter. The tips extend 2 mm from their supports and 10 mm in total from the main shafts of the probe that is 3 mm in diameter

been characterized experimentally for a static interface with no curvature, following a procedure detailed in Cartelier (1990). For the tips of the probe used for this work, it is 0.50 mm.

3.1 Optical probe data processing

When the photodetector signal voltage was greater than a prescribed threshold, the gas characteristic function was set to one; otherwise, it is set to zero. The void fraction was based on the time average of the characteristic function of the tip. The time corresponding to the maximum value of the cross-correlation function (based on the two gas characteristic functions of the probe tips) was representative of the most probable transit time of the gas between the two tips, t_{aP}. The transit time is defined as the time difference between the times indicating the beginning of the gas structure detection on each tip. Thus, a most probable gas velocity was obtained as $U_{aP} = l_{12}/t_{aP}$. The signal from a transient gas structure was recognized as an associated gas structure if the signals from the two tips had a time delay (corresponding to transit time) that was within a time window around the most probable transit time, t_{aP}. The velocity of different associated gas structures U_a was deduced based on l_{12} and the transit time.

The mean velocity $\overline{U}_a$ and its RMSD value were deduced by weighting the velocity of each associated gas structure by its residence time measured on the upstream tip. The determination of the velocity distribution by this method is well suited for unidirectional flow (reverse or not), but it is not appropriate for the flow of high void fraction (>90 %). Indeed, for high void fraction in the air cavity or air layer, it was difficult to extract a most probable transit time from the cross-correlation function.

In general, when a gas bubble is pierced by the tip, the bubble center does not cross the tip. Thus, the bubble is not expected to intersect the tip along its diameter, but along a shorter length, which is called the chord length. The chord length l_c of each associated gas structure (bubble) was obtained as the product of its velocity and its residence time on the upstream tip (upstream relative to the local direction of the flow). This made it possible to determine the bubble chord length distribution.

When the probe was immersed in a bubbly flow, the inverse method developed by Clark and Turton (1988) was used to determine the bubble size distribution. This method was applied successfully in Gabillet et al. (2002), for the case of bubble injection along a wall, for bubbles $O(1\ \mathrm{mm})$ and void fraction less than 30 %. This method is based on joint probability density functions that give the likelihood of measuring a specific chord length for a given bubble size, and it requires an assumption on the bubble shape

(eccentricity). It also assumes that the largest chord length detected is equal to the largest bubble major axis diameter to be found in the bubble size distribution. Assumptions of both spherical and ellipsoidal bubbles, with varying eccentricity ratios, were tested.

3.2 Uncertainties of the measurement

These measurements are sensitive to the voltage threshold levels applied when building the characteristic function. If $v_{\min}$ and $v_{\max}$ are the voltage levels obtained in the liquid and gas, respectively, then varying the voltage threshold level in the range $[v_{\min}, v_{\min} + (v_{\max} - v_{\min})]$ leads to a significant variation of the measured void fraction value that can be modeled by Eq. 12. In this relation, it is assumed that the error in the residence time determination is the same for each gas structure and is equal to the time of the dewetting process of the tip (i.e., l_L/U_a). This leads to an error in the void fraction determination representative of the ratio between the latency length and the chord length of the gas structures:

$$\left(\frac{\Delta\alpha}{\alpha}\right) \approx \pm\frac{n_b l_L}{2\alpha T\overline{U_a}} \approx \pm\frac{l_L}{2\overline{l_c}}. \tag{12}$$

Assuming that the voltage difference in the gas and liquid is the same for the two tips and that the gas structure is pierced by the two tips in the same way, the uncertainty in the velocity measurement due to the threshold level is a systematic error that compensates if the two tips have the same latency length and yields

$$\left(\frac{\Delta U_a}{U_a}\right) = \pm\frac{|l_{L1} - l_{L2}|}{2l_{12}}. \tag{13}$$

The uncertainty in the chord length determination results from the combination of errors in void fraction and gas velocity determination given by

$$\left(\frac{\Delta l_c}{l_c}\right) = \left(\frac{\Delta U_a}{U_a}\right) + \left(\frac{\Delta\alpha}{\alpha}\right). \tag{14}$$

In addition, we can write the uncertainties in void fraction and velocity linked to the sampling frequency as

$$\left(\frac{\Delta\alpha}{\alpha}\right) \approx \pm\frac{2n_{\mathrm{b}}}{\alpha T f_e} \tag{15}$$

$$\left(\frac{\Delta U_a}{U_a}\right) \approx \pm\frac{2U_a}{l_{12}f_e} \tag{16}$$

where n_{b} is the bubble number and T is the measurement time.

The relative uncertainty in the determination of void fraction and chord length due to the sensitivity to the voltage threshold level was estimated based on Eqs. 12 and 14. It was less than ±20 %, and it was decreasing (relative uncertainty less than 5 %) for high void fraction ($\alpha > 30$ %) associated with longer residence time. Assuming that the error in the determination of the residence time is maximal, this uncertainty is overestimated. For the gas velocity, the sensitivity to the threshold value in the range $[v_{\min} + 0.30(v_{\max} - v_{\min}),\ v_{\min} + 0.70(v_{\max} - v_{\min})]$ was examined. Regardless of the void fraction value, the relative uncertainty due to the voltage threshold was less than ±3 % for the gas velocity determination.

The transit time window, used to associate gas structures of the two tips, was chosen so as to have a velocity distribution centered on $U_{aP} = [(1 - \beta)|U_{ap}|, (1 + \beta)|U_{ap}|]$. A value of $\beta = 0.48$ was applied to avoid truncated velocity distributions or double-peak velocity distributions. Sensitivity of the gas mean velocity to the transit time window was investigated, and the relative uncertainty was found to be less than ±12 %. The sampling frequency, f_e, was set to 50 kHz. Based on Eqs. 14, 15, and 16, this sampling frequency leads to a possible relative error of ±5 %, ±6 %, ±11 % for the determination of the void fraction gas velocity and chord length, respectively.

The measurement time required depended on the void fraction. However, for all flow conditions considered, it was 30 or 60 s to ensure at least 300 gas structures were detected on each tip near the wall. The convergence of the data as a function of the number of associated gas structures was examined, and for 100 associated gas structures, the mean value of the velocity was accurate to within 2 % (with 68 % confidence level).

Repeatability between the different experiments was explored also. The RMSD value was less than 20 % of the mean value for the void fraction, and less than 5 % of the mean value for the velocity. RMSD values of the void fraction were higher at the edge of the cavity when it was filled with air. The RMSD value of the mean velocity was larger further from the wall where there was a change in the sign of the velocity (edge of the reverse flow). To compensate for errors of reproducibility, the void fraction and the mean velocity were averaged among several runs (between 3 and 8 runs).

The optical probes were attached to a traverse mechanism described in Mäkiharju (2012). The traverse enabled the probes to be positioned with accuracy of at least 0.2 mm. However, the absolute position relative to the model was only accurate to within ±0.7 mm, as the tips could not be allowed to touch the model surface, and it was not possible to access the inside of the water tunnel with both the model and probes installed. For each flow condition investigated, the accuracy of the void fraction and velocity measured by the probes is indicated by error bars included in the first plot containing the data.

4 The partial cavity flow

4.1 The recirculating water channel

The X-ray system was designed for use with an existing cavitation tunnel at the University of Michigan. However, a new test section, 864 mm long with a $(209.6\ \text{mm})^2$ cross-section and 28.6 mm chamfer in the corners, was constructed for these experiments. Test section windows 152 by 864 mm were used to provide good optical access. The windows were made as thin as 1 cm, to reduce the baseline X-ray attenuation. In the empty test section, the flow can achieve speeds in excess of 18 m/s, while the pressure can be varied from that below vapor pressure to over 200 kPa. Additional details of the flow facility are provided by Oweis et al. (2004).

4.2 The test model and flow conditions

The test model was a flat plate that spanned the width of the test section, $W = 209.6$ mm, and had an overall length of $L = 910$ mm. The model had a backward-facing step of height $H = 12.7$ mm and was located 350 mm from the leading edge. The boundary layer upstream of the cavity separation was tripped at the leading edge of the 2:1 ellipse. Air was injected from the base of the step through a 4.7 mm tall slot spanning the width of the model. The plate thickness downstream of the step was 19.1 mm. The air was introduced first into a chamber inside the model and exited the chamber through a porous plate to produce a spanwise uniform flow. The spanwise uniformity of the air injection was measured using a hot-wire anemometer and was found to be uniform within the accuracy of the measurement. An upstream gate was used to form a free surface above the model, enabling air removal during long periods of air injection. Figure 10 shows a schematic diagram of the model and free-surface-forming gate in the test section.

The free-stream speed for each condition was measured via a Pitot tube placed in the flow at the spanwise centerline with its tip $17H$ upstream of the backward-facing step and $\sim 2H$ from the step's surface, with the pressure difference measured with an Omega Engineering PX2300-5DI, 0–5 psi differential pressure transducer. The free-stream flow velocity, defined as the bulk flow speed at the position of flow separation above the backward-facing step, was $U = 1.80 \pm 0.05$ m/s for all data discussed in this paper. The pressure in the test section was kept nominally at 1 atm via vents to the atmosphere. The transducers were connected to a National Instruments DAQ NI USB-6259, and signal processing and recording were performed using Labview 2009 Virtual Instruments. The injected gas flow rate, Q, was measured with two flow meters. For flow rates to 7.97×10^{-6} m^3/s, the flow meter used was the Omega Engineering FL-2001 with manufacturer specified accuracy of $\pm 0.39 \times 10^{-6}$ m^3/s. For flow rates above 7.97×10^{-6} to 3.93×10^{-5} m^3/s, the flow meter used was Omega Engineering FL-2003 with manufacturer specified accuracy of $\pm 0.20 \times 10^{-5}$ m^3/s. The water was tap water filtered through a 5 micron particulate filter, and its temperature was maintained at 25.0 ± 1 °C, except for the high-speed video that was recorded previously when the water temperature was 18.0 °C.

High-speed video of the flow was recorded using a Vision Research Phantom v710 camera and two Arri-studio lights. However, only at the lowest air fluxes were the individual bubbles distinguishable (i.e., minimal overlap when viewed from below). Several hundred independent frames were processed manually, to obtain the bubble size, minor-to-major axis ratio, and velocity histograms. Assuming that the bubble edge location was measured correctly within ± 1 pixel, the diameter measurement is accurate within ± 0.12 to 0.2 mm. The usual displacement over the time differential was greater than 50 pixels; thus, the velocity can be assumed accurate within ± 0.04 m/s. In total, 1,236 bubbles were measured. Also, the void fraction, as a function of distance from the test surface, could be estimated as the depth of field was known, and the flow was assumed to be nominally two-dimensional.

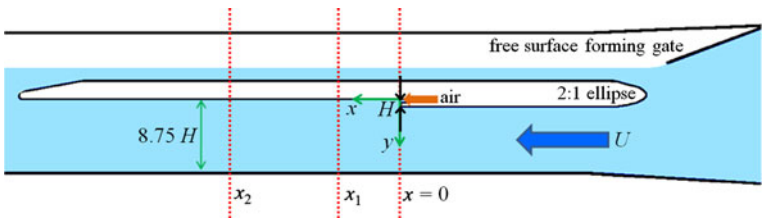

Fig. 10 A schematic diagram of the test model used to form the cavity along with the primary measurement locations. The test model spanned the test section and consisted of a plate with leading and trailing edge treatments, along with a backward-facing step of height $H = 12.7$ mm. Air was introduced from the base of the step. A free-surface forming gate was located immediately upstream of the model. As shown, the origin of the coordinate system is located at the base of the backward-facing step. Optical probes were deployed center-span at two streamwise locations, $x_1 = 5H$ and $x_2 = 21H$. The X-ray system was used to measure the void fraction distributions at locations spanning $-1.5 < x/H < 21$

4.3 The single-phase flow in the vicinity of the backward-facing step

To characterize the inlet boundary conditions, the turbulent boundary layer upstream of the backward-facing step near the location of flow separation was measured using two-dimensional particle image velocimetry. The system was comprised of a LaVision FlowMaster 3s camera, New Wave Gemini 200 lasers, external LaVision PTU 9 timing unit, and a PC running LaVision's DaVis 7.2. At the flow speed of 1.8 m/s, the boundary layer upstream of the step was turbulent and conformed to a 1/7th-velocity profile with thickness $\delta = 7$ mm and momentum thickness $\theta = 0.8$ mm, yielding $Re_\theta = 1{,}400$.

Additionally, the single-phase flow downstream of the backward-facing step was measured. The length of the single-phase separation bubble was found to be approximately $6.5H$, which is consistent with the historical value for the case of a low expansion ratio, 1.13 in this case (Adams and Johnston, 1988).

4.4 X-ray, optical probe, and video measurement locations

Measurements of the cavity flow were collected in two distinct flow regions. The first region was between $0 < x/H < \sim 7$, which corresponded to the closure region of the partial cavity. Here, x is the streamwise distance from the step and H is the step height. The second region beyond $x/H = 8$ corresponded to the bubbly flow in the cavity wake. The X-ray images were acquired with three different fields of view that extended from $-1.5 < x/H < 9$, $1 < x/H < 11.5$, and $11 < x/H < 21$. The optical probe measurement locations are indicated in Fig. 10 and were $x/H = 5$ and $x/H = 21$. The high-speed video was recorded for $10 < x/H < 19$.

5 Results

5.1 Partial cavity flow

Figure 11 shows two images of the partial ventilated cavity. Figure 11a is an oblique view from below, and Fig. 11b is an elevation view of the cavity for $U = 1.8$ m/s and $Q = 2.2 \times 10^{-5}$ m^3/s. Therefore, the non-dimensional gas flux, $q = Q/UHW = 4.6 \times 10^{-3}$. The free surface was detached cleanly from the apex of the backward-facing step, and a nominally two-dimensional gas cavity formed downstream. The gas cavity closure occurred at $x/H = 6.5 \pm 0.5$, which compares well with the location of the single-phase cavity closure of $x/H \sim 6.5$ (Adams and Johnston 1988). Additionally, the interface of the cavity had small waves associated with the ingestion of the turbulent boundary layer upstream of the cavity closure.

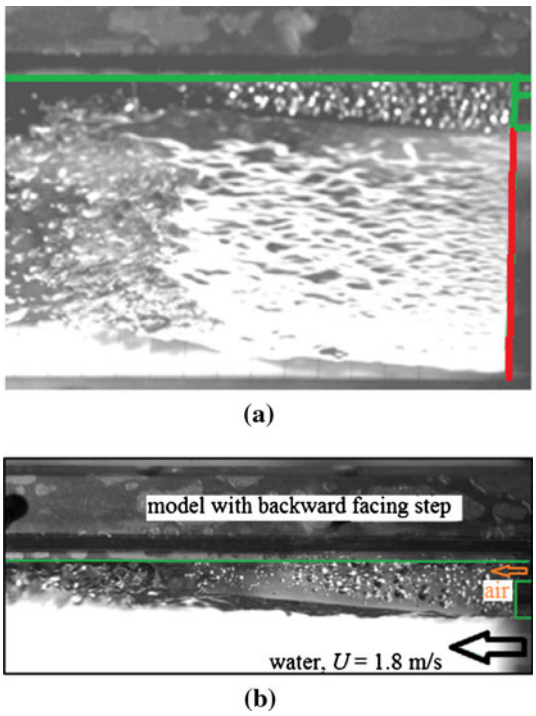

Fig. 11 The air cavity formed at the backward-facing step viewed at an oblique angle from below (**a**) and from the side (**b**) for $U = 1.8$ m/s, and $Q = 2.2 \times 10^{-5}$ m^3/s ($q = Q/UHW = 4.60 \times 10^{-3}$). The *green lines* outline the *bottom* of the model as well as the backward-facing step. The *red line* highlights the spanwise edge of the step where the flow separates

The cavity closure was nominally two-dimensional. The gas was entrained into the cavity wake as ligaments of gas that were stretched and then divided into bubbles. Some of the bubbles were advected immediately downstream, while others briefly remained in the recirculating flow region of the cavity closure. This resulted in a bubbly flow, with thickness on the order of the cavity thickness, advected from the cavity closure.

5.2 Cavity closure region

Figure 11 shows the cavity near the backward-facing step for $q = 4.6 \times 10^{-3}$. The void fraction was essentially 100 % within the cavity upstream of $x/H \sim 3$, but due to multiple scattering (reflection and refraction), it could not be estimated in the closure region based on visible light images alone, which is a problem similar to those in many cavitating flows. Hence, the X-ray system was used to measure the void fraction in the closure region, and the results are presented in the following.

Figure 12a shows a raw false color (i.e., a colored 8-bit gray scale image) X-ray image of the partial cavity. This 8-bit representation of light intensity is related to

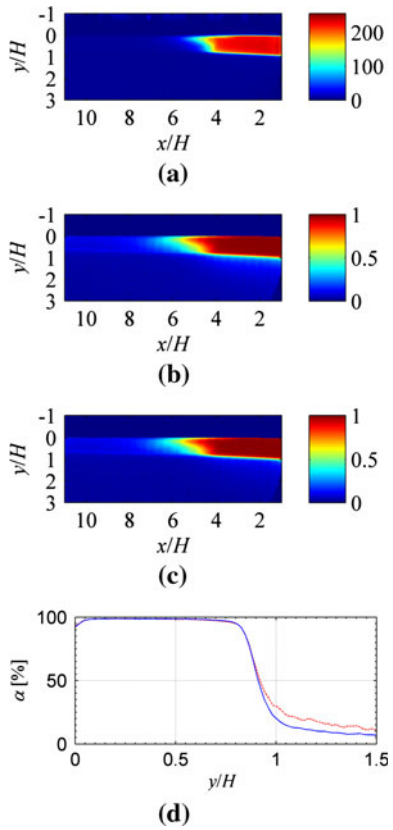

Fig. 12 Images of the cavity recorded with the X-ray densitometry system. **a** A false color X-ray image of the partial cavity (the *color* scale represents the average *grey* scale value varying between 0 and 255); **b** the resulting void fraction distribution; **c** the void fraction distribution corrected for veiling glare; and **d** effect of the veiling glare correction. *Vertical* profiles of the void fraction through the cavity interface at $x = 2.5H$ before and after the correction for the veiling glare, shown by *red dashed* and *blue solid lines*, respectively

attenuation of the X-ray beam and hence yields a quantitative measure of the void fraction. Figure 12b shows the void fraction distribution, and near the bottom of the cavity where we had a sharp 100 to 0 % void fraction change; the effect of veiling glare can be seen clearly. Figure 12c exhibits the image corrected for veiling glare. Although little change was evident, the affect can be clearly seen in Fig. 12d that compares the uncorrected and corrected distribution at $x/H = 2.5$. The veiling glare correction is imperfect, and some smearing of the interface persists due to the non-parallel beam paths, but the post-processed image is improved. The 2D projection of the void fraction distribution revealed the existence of strong gradients in the cavity closure region. Figure 13 shows the local profile of void fraction perpendicular to the flow boundary, y/H, at different streamwise locations, x/H, for $q = 1.64 \times 10^{-3}$, $q = 4.60 \times 10^{-3}$ and $q = 8.21 \times 10^{-3}$.

To obtain data for comparison with the X-ray measurements, an optical probe was placed in the closure region at $x/H = 5$. Figure 14 presents the measurement of local void fraction and mean gas interface velocity based on the dual-tip optical probe with varying position, y/H, from the flow boundary for $q = 1.64 \times 10^{-3}$, $q = 4.60 \times 10^{-3}$, and $q = 8.21 \times 10^{-3}$. We observe that the tip upstream of the local flow always recorded a higher void fraction, as the second tip was in the wake of the first and some bubbles could be deflected from the probe. (Indeed, the downstream probe detects 10 % fewer gas structures than the upstream probe, in agreement with deflection by the tip located upstream.) More deflection was encountered at the edge of the recirculating region (20 %) where the streamwise velocity was weak. We also note the large error bar for the void fraction in Fig. 14b at $y/H \sim 0.35$. This is due to the uncertainty in the void fraction determined based on Eq. 12, where we can see that the uncertainty increases for low velocities, such as those encountered in the recirculating region. These data are compared to X-ray data in Sect. 5.4.

Figure 14d shows the velocity profiles in the closure region of the cavity, which align well for $q = 4.60 \times 10^{-3}$ and $q = 8.21 \times 10^{-3}$. For $q = 4.6 \times 10^{-3}$, the velocity profile exhibits clearly the recirculation in the near-wall region of the cavity. The edge of the recirculating region was associated with a local increase in the void fraction. For the maximum air flow rate, the cavity was completely filled with air ($\alpha \sim 100$ %), and thus, the algorithm would not be able to associate with the gas structures on the two tips. Hence, the velocity was not plotted for $y/H < 0.7$.

Figure 15a and b exhibit the bubble size and velocity histograms, respectively. These data are for $q = 4.60 \times 10^{-3}$ at $x/H = 5$, and $y/H = 0.615$. The mean bubble diameter was 1.92 ± 0.07 mm (RMSD value). The number of bins for the bubble size histogram determination is limited by the inverse method that can lead to empty classes or negative values of the probability function if the number of associate bubbles is too small. The smallest detected bubbles approached the limit of what is detectable with the optical probe ($\sim$0.5 mm). The vast majority of the bubbles were O(1 mm), and these were not individually detectable by the current X-ray system; however, their cumulative contribution will significantly affect the X-ray attenuation.

5.3 Bubbly flow in the cavity wake region

In the wake region with the lowest gas flux, it was possible to measure the bubble velocity and size distributions directly from video of the flow, and this could be compared against the optical probe data. Figure 16a shows a photograph of the bottom view and Fig. 16b a photo of the side view. All results from the high-speed video are for 1.8 m/s speeds with ventilation rate $q = 1.64 \times 10^{-3}$. We note that the Weber number, $\rho_w U^2 d/\sigma$, based on the bubble major axis and nominal free stream speed of 1.8 m/s would

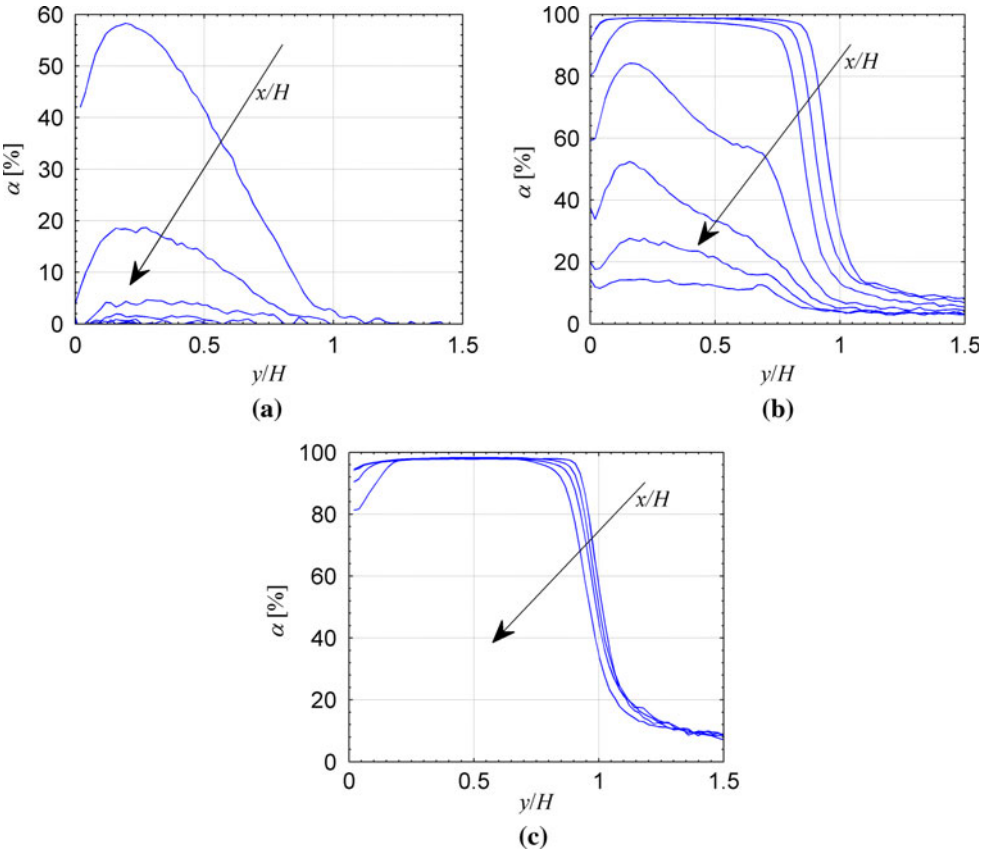

Fig. 13 Void fraction profiles based on the X-ray measurement downstream of the step as a function of distance from the surface, *y/H*. **a** $q = 1.64 \times 10^{-3}$, **b** $q = 4.60 \times 10^{-3}$, and **c** $q = 8.21 \times 10^{-3}$. For **a** and **b,** the first profile is recorded approximately $x = 1.5H$ from the step and each *curve* represents the profile one H apart. Profiles in **c** start approximately from $x = 0$, each $2H$ apart. The dip in void fraction of one of the *curves* extending from $y = 0$ to $0.2H$ in **c** is caused by droplets that were clinging to the plate in the all air calibration image, hence locally causing an offset in calculated void fraction

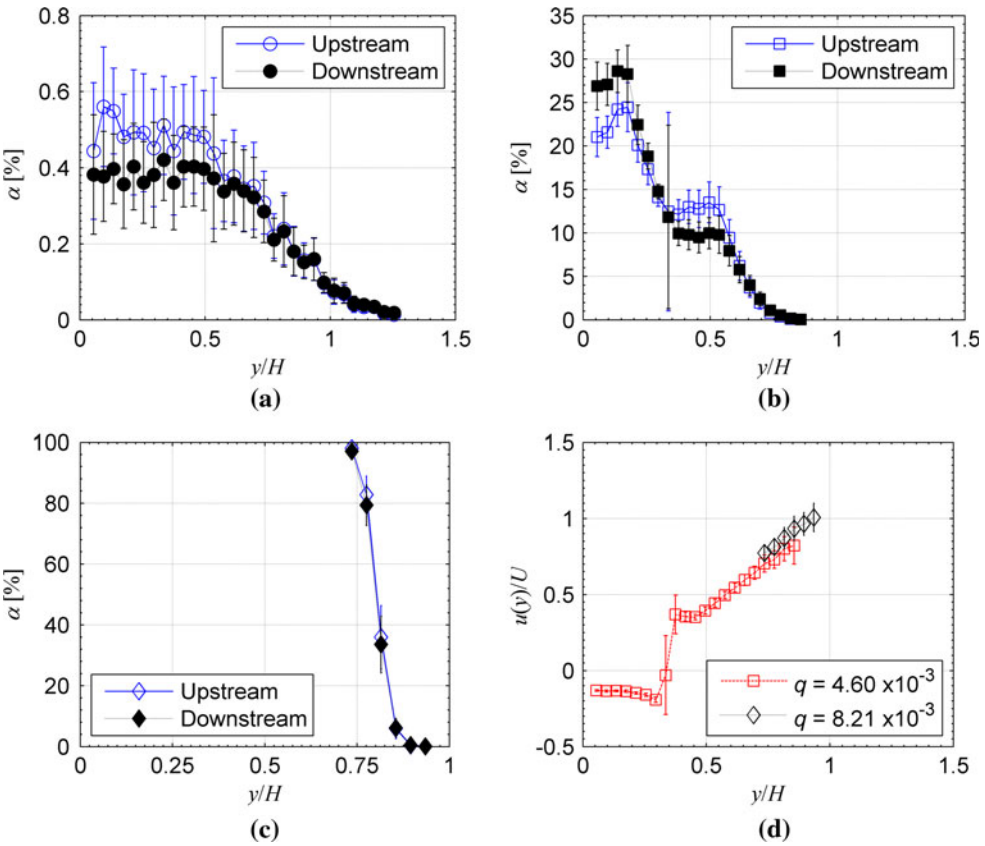

Fig. 14 The local void fraction measured by the two tips of the optical probe at $x/H = 5$ for varying *y/H*. **a** $q = 1.64 \times 10^{-3}$, **b** $q = 4.60 \times 10^{-3}$, and **c** $q = 8.21 \times 10^{-3}$. **d** The local mean velocity of the bubbles based on optical probe data for $q = 4.60 \times 10^{-3}$ and $q = 8.21 \times 10^{-3}$. The *error bars* of the void fraction account for the threshold sensitivity, the sampling rate sensitivity, and repeatability error based on the RMSD value for several runs divided by the root square number of runs. *Error bars* of the mean gas velocity take into account the threshold sensitivity, the sampling rate sensitivity, the time convergence error based on the number of gas structures associated, and the repeatability error based on the RMSD value obtained for the different runs divided by the root square of the number of runs

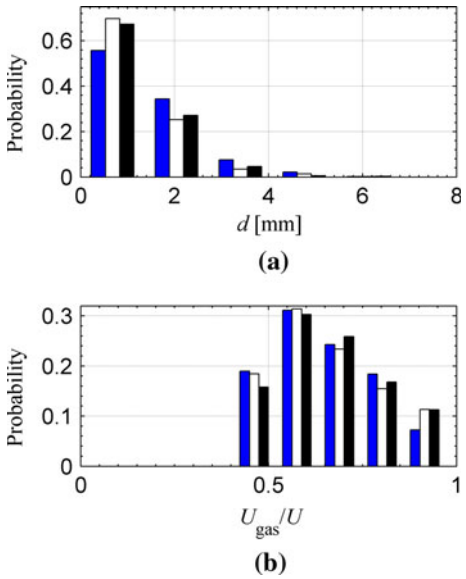

Fig. 15 **a** Bubble size *histograms* and **b** bubble velocity *histograms* at $x = 5H$ and $y = 0.615H$ for $q = 4.60 \times 10^{-3}$ and three different runs of 30 s showing the reproducibility. The mean bubble size based on the bubble size *histogram* obtained by the inverse method is 1.9 mm

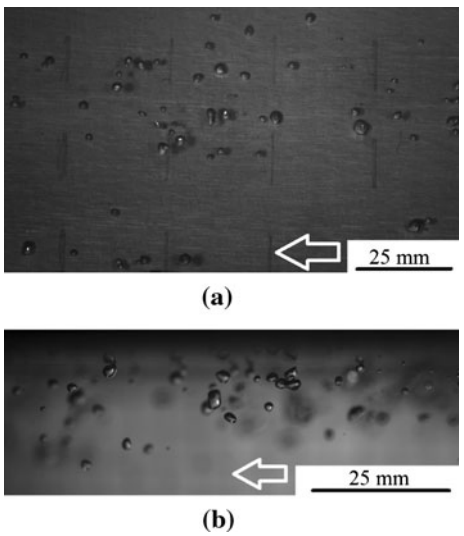

Fig. 16 Photographs from a 1,000 fps movie showing the bubbles in the vicinity of the optical probe position, $x = 21H$ as viewed from *below* (**a**) and from the *side* (**b**). Note that, the scales in each image are *different*

be $O(100)$, for a typical 2 mm diameter bubble, and hence, many of the bubbles are likely to be ellipsoidal, as evident in Fig. 16b. To demonstrate this more clearly, Fig. 17 shows the eccentricity ratio histogram from the video, and also compares the bubble size and velocity histograms to the ones obtained from the optical probes. Obviously, Fig. 17a shows that the bubbles were predominantly ellipsoidal. In Fig. 17b, we can see that only the largest

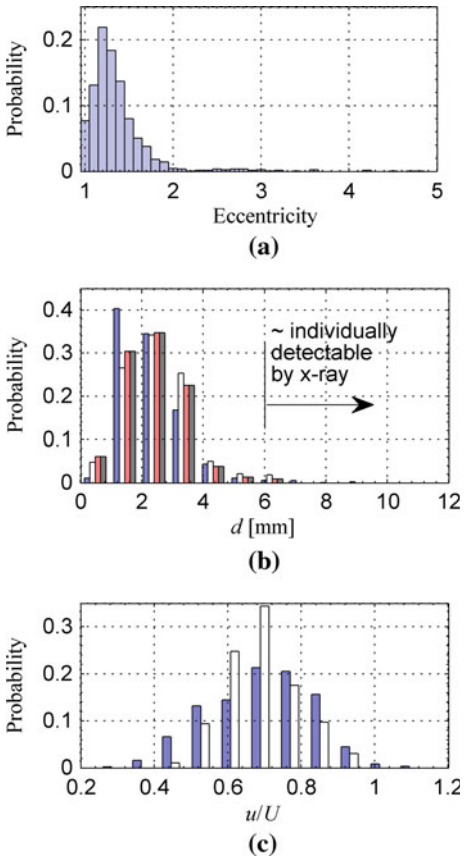

Fig. 17 **a** Bubble major and minor axis ratio eccentricity ratio *histogram* based on data from video show that most bubbles were slightly elliptical. **b** Bubble size *histogram* based on both optical probe and video data at $x \sim 21H$ and $q = 1.64 \times 10^{-3}$. Video data are shown by the first *bars*. The second, third, and fourth *bars* show the optical probe data at $y = 0.134H$ based on the assumption that eccentricity is a function of the major axis diameter (function deduced from video recording), eccentricity equal to 1 and 1.31, respectively. The mean bubble major axis is 2.26 mm. Also shown is the approximate size of the larger individual bubbles detectable by X-ray. **c** The bubble velocity *histograms* obtained from video and optical probe data, as shown by the first and second *bars*, respectively

bubbles are individually detectable from single X-ray frames. (While the smallest bubbles are not individually resolvable from unsteady data, these more numerous smaller bubbles contributed to the overall time-averaged void fraction measured via X-ray.) For the optical probe data, different models of eccentricity were tested, based on the eccentricity ratio that is available from the video recording.

Figure 17b shows histograms based on three different assumed eccentricity ratios. The mean actual eccentricity ratio was around 1.31. Implementation in the inverse method of different values for the eccentricity ratio (1, 1.31, and a fit as a function of the major axis) leads to very similar bubble major axis histograms measured by the optical probe, as shown in Fig. 17b. The mean bubble size based on video and optical probe data was 1.86 and

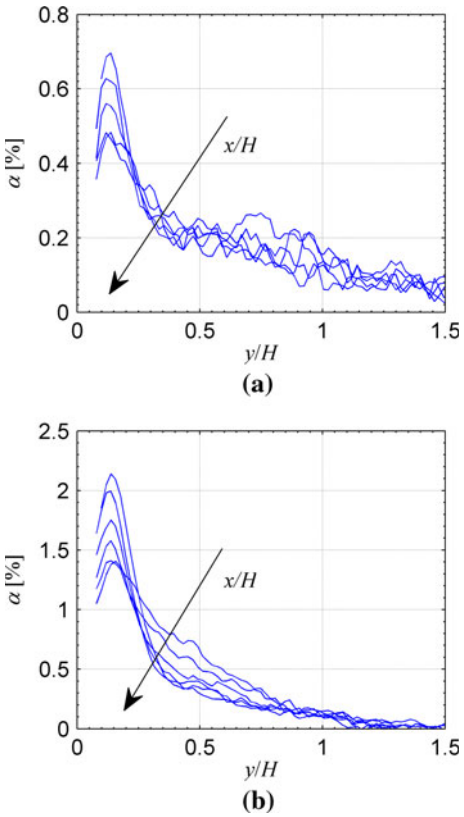

Fig. 18 The percent void fraction profiles in the cavity wake for **a** $q = 1.64 \times 10^{-3}$ and **b** $q = 4.60 \times 10^{-3}$. The first profile was recorded approximately $x = 11H$ from the step, the second profile was recorded $12H$ from the step, and each sequential *curve* represents the profile at $2H$ intervals

2.26 mm, respectively. The mean velocity, U_a/U, based on video and optical probe data was 0.64 and 0.68, respectively. The bubble size and velocity histograms show a small difference in the bubble populations based on video and based on optical probe data. Also, the bubble population based on optical probe data was not affected strongly by the assumed bubble eccentricity used in the data processing.

The void fraction in the wake was on the order of 1 %, and thus for these measurements, the X-ray source settings were adjusted to achieve improved contrast, as it was possible to use higher beam intensity without saturating the imager. A 12.7 mm container fixed between the source and the object could be filled and emptied to obtain reference intensities G_a and G_w, where 100 % void fraction was defined as when the test section was full and the container empty. The container was then maintained full during data acquisition. Figure 18 shows the void fraction distribution based on X-ray measurement for $q = 1.64 \times 10^{-3}$ and $q = 4.60 \times 10^{-3}$. Even at these low void fractions, where noise in the measurement becomes more significant, the streamwise evolution of the void fraction distribution is evident. To ensure that the X-ray provided reliable data in this challenging low void fraction flow, the dual-fiber optical probe data were used for comparison. Figure 19 shows the local void fraction and mean gas velocity profiles obtained by the optical probe at $x/H = 21$. By comparison with the cavity closure region, the air layer at the highest gas flux became thinner, whereas the bubbly layer at the smaller gas fluxes extends further. While the void fraction data can be compared directly to those obtained by X-ray, the velocity information can be used to calculate the total gas volume flow rate based on void fraction measurements from both techniques. This can then be compared to the injected gas flow rate measured by the rotameters.

5.4 Comparison of the X-ray, optical probe, and video measurements

The void fractions measured with the X-ray system and with the optical probe at $x/H = 5$ are compared in Fig. 20. The same behaviors are clearly observable, as the distributions peak near $y/H \sim 0.2$ and exhibit a near plateau around $y/H \sim 0.5$. However, the data do not match; in fact, any small deviation in flow conditions or measurement location mismatch would have a large effect due to the rapid streamwise evolution seen in Fig. 13b. The X-ray measurement is also affected by the imperfectly corrected veiling glare, non-parallel beam paths, and signal noise. For the optical probe data, it should be noted that the presence of the probe itself can perturb the flow, especially where reverse flow occurs such that the probe is influenced by its own wake. A reverse flow can be seen in Fig. 14d, and data in Fig. 14b could be affected by the flow perturbation caused by the probe. In this same figure, the effect of the local flow direction is clear, and the measurement performed by the probe upstream relative to the local direction of the flow is more representative of the void fraction. Indeed, the probe downstream always records a lower void fraction. This is caused by some of the bubbles being deflected in the wake of the upstream probe. The probe can induce deformation of the bubbles, local deceleration, and bubble deflection (bubbles avoiding the tips, including the upstream tip relative to the local direction of the flow). Julia et al. (2005) has characterized the contribution of these different effects to the void fraction measurement for bubble diameter between 3 and 5 mm and for flow velocity between 0.22 and 0.28 m/s. For these flow conditions, they highlighted that deflection and deceleration effects compensate for each other. The deformation effect is the most prominent and can lead to an underestimation of the void fraction by as much as 50 % of the local void fraction value.

Figure 21a and b show a comparison of the average void fraction profiles obtained from optical probes, X-ray, and

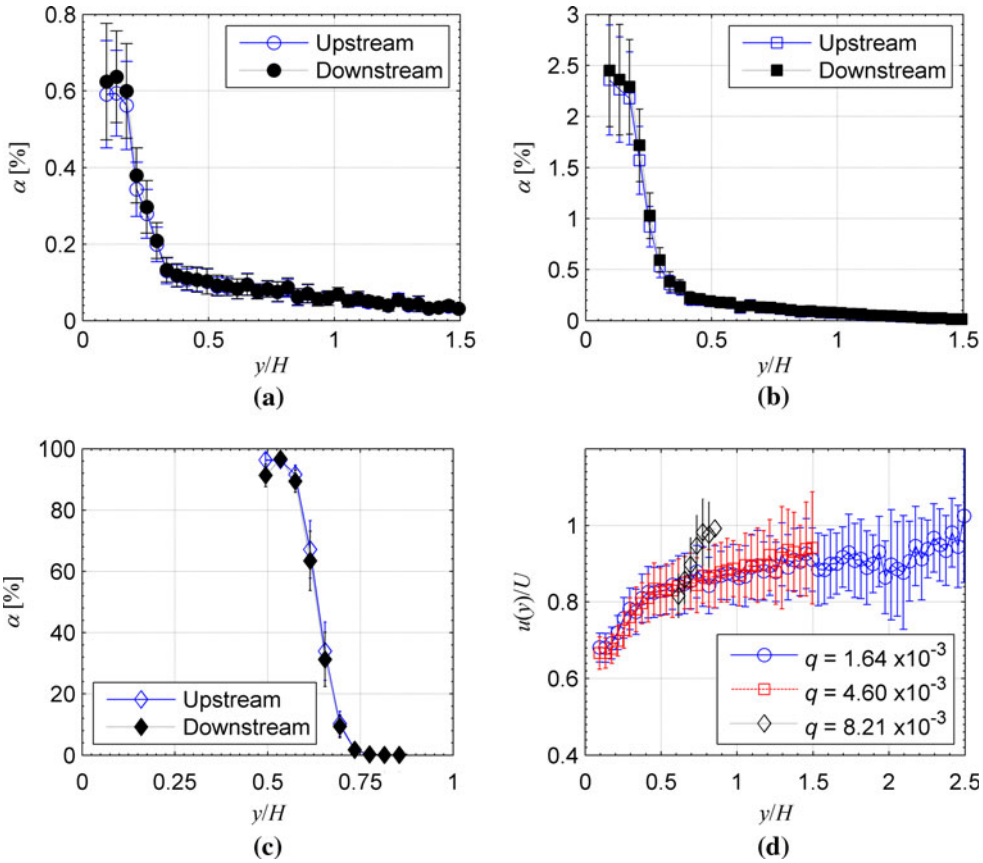

Fig. 19 The local percentage void fraction measured by the two tips of the optical probe at $x = 21H$. The non-dimensional gas flux was **a** $q = 1.64 \times 10^{-3}$, **b** $q = 4.60 \times 10^{-3}$, and **c** $q = 8.21 \times 10^{-3}$. **d** The streamwise velocity of the gas phase derived from the optical probe at $x = 21H$. The *error bars* account for the factors discussed in conjunction with Fig. 14

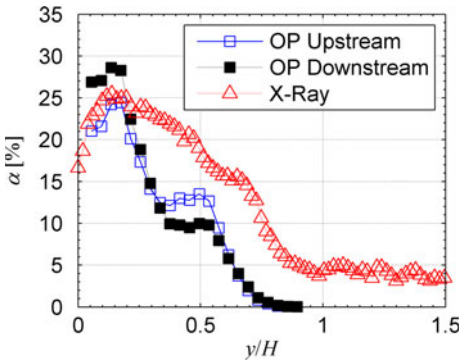

Fig. 20 Comparison of the percent void fraction measured near the cavity closure at $x = 5H$ using X-ray and optical probes data. Data are for $q = 4.60 \times 10^{-3}$. The *error bars* for the optical probe data were shown in Fig. 15b and are $O(2\ \%)$. For the X-ray data, the standard deviation of the mean in the region of interest was at most 0.74 % and had an average of 0.26 %. However, the actual uncertainty of the X-ray data is determined by the numerous factors discussed in the text. Most notably, the cavity closure was to a degree three-dimensional, and due to the high void fraction gradient, the effect of non-parallel beam paths was more significant. As the data available do not facilitate accurate assessment of error due to the 3D nature of the cavity closure, the X-ray *error bars* are not included

video (only in 21a) at $x/H = 21$. For the video data, the number of bubbles was insufficient for convergence, as random fluctuations in the distribution are apparent. Given the increasing uncertainty of the measurement at the low void fractions, scatter, limited averaging time of the X-ray dataset used, veiling glare, non-parallel beam paths, etc., the agreement is quite satisfactory. Also, due to the streamwise evolving void fraction profiles, any positional uncertainty of the X-ray compared to the optical probe will contribute to a difference between the profiles. As seen in Fig. 18, we observed that the void fraction profile in this region is still evolving, but much less dramatically than in the cavity closure region.

The comparisons to optical probes, issues related to veiling glare, and non-parallel beam paths are discussed in more detail in Mäkiharju (2012), but these data illustrate a measure of the capability of the system used in this study. With the X-ray measurements, it is possible to quantitatively describe and to gain new insight into the physics of the fluctuations, cavity breakup, and bubble shedding at various flow conditions.

Finally, Table 1 presents the injected gas flow rate compared to that calculated based on optical probe and X-ray data assuming fully 2D flow. Figure 19d had showed the velocity as a function of distance y/H, as measured by the dual-tip optical probe. Knowing the velocity profile and using the optical probe and X-ray densitometry void fraction data, the gas volume flow rates are calculated from

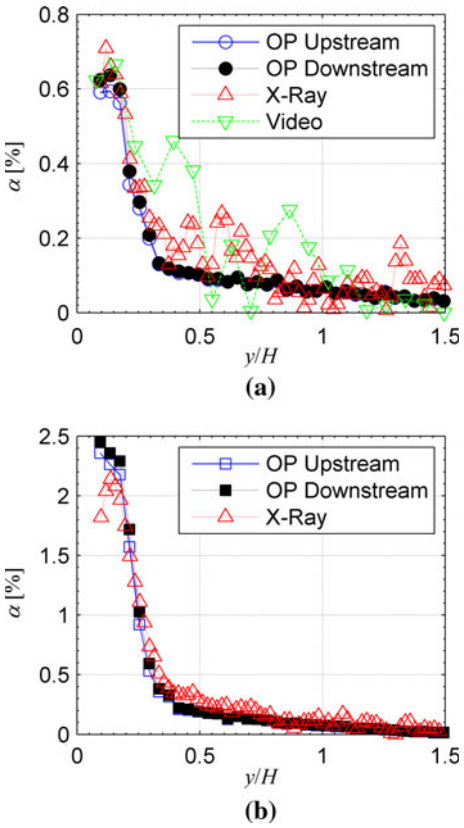

Fig. 21 **a** A comparison of the measured void fraction by all three methods for $q = 1.64 \times 10^{-3}$ at $x = 21H$. **b** Comparison of the void fraction based on the optical probe and X-ray data for $q = 4.60 \times 10^{-3}$ at $x = 21H$

$$Q = \sum_{j=1}^{J} \Delta y u(y_j) \alpha(y_j) W. \quad (17)$$

here, W is the span of the model, 209.6 mm, Δy is the measurement location spacing normal to the model surface, $u(y)$ is the flow speed parallel to the model surface measured with the optical probe, and α is the local void fraction. (The upstream measurement location was within the complex recirculation region where the presence of the optical probe more likely affected the flow, and hence, a similar comparison was not attempted for data from that position.)

Table 1 Volume flow rates of air based on the flow meter, optical probe, video, and X-ray measurements at $x \sim 21H$

Injection rate q_{inj}	Optical probes q_{OP}/q_{inj}	Video q_{video}/q_{inj}	X-ray $q_{X\text{-ray}}/q_{inj}$
1.64×10^{-3}	1.09	1.05	1.32
4.60×10^{-3}	1.01	N/A	1.01
8.21×10^{-3}	Air layer	N/A	Air layer

To get the volume flow rate from the X-ray measurement, the void fraction data were integrated from $y = 0$ to $1.48H$. Both the void fraction and velocity were set to zero at $y = 0$. Flow speed, $U = 1.8$ m/s

In Table 1, we observe that the volume flow rate was overestimated at the lowest gas flux, especially by the X-ray. The reason for this overestimate can be understood readily by revisiting the void fraction distributions presented in Fig. 21. Therein we see that the void fraction is overestimated at values below 0.4 %. Besides the possible effect of short averaging times and veiling glare of the X-ray images, at these low void fractions, the calculated value is extremely sensitive to the smallest error in any of the light energies as can be seen from Eq. 4. However, as the gas flux is increased, the relative uncertainty is reduced, and the gas flux calculated from the X-ray data moves closer to the injected value.

6 Conclusions

We have demonstrated how time-resolved X-ray densitometry can be successfully used to measure the volume fraction fields for nominally two-dimensional flows, and this system was demonstrated on a canonical flow: a cavity forming at the base of a backward-facing step and the bubbly flow in its wake. The current system described here can quantitatively measure the time-averaged two-dimensional projections of 0 to 100 % void fraction to within 2 %, distinguishing features of O(1 mm), and detecting changes at time scales on the order of 1 ms through an enclosed domain of a gas/water mixture that is $\sim$21 cm thick.

Video and optical probe measurements were compared to the X-ray data. The agreement between measurements of volume fraction using the optical probe and X-ray data yielded satisfactory agreement within understood levels of uncertainty. In particular, this was the case for unidirectional flow at $x/H = 21$, where the optical probe perturbs the flow the least and where the void fraction was above 0.5 %, conditions that are optimal for each measurement method. In this case, the void fraction profiles measured using the X-ray system showed the best agreement with those obtained with the optical probes. The gas volume flux derived from video, bubble probe, and X-ray data compared well with the known amount of injected gas.

We note that the X-ray acquired data quite rapidly in comparison to the point probes. To acquire the void fraction profiles shown in Figs. 14 and 19 using the optical probes required two hours for each condition. The X-ray data required only a few seconds per condition and also provided information on the streamwise evolution of the void fraction. Given that the X-ray had better than 1 mm spatial resolution, using any point probe (such as the optical probe) would require more than eight days of

continuous operation to acquire the same spatial distribution (assuming three minutes per point covering an area 30 mm × 140 mm, with points every 1 mm).

The X-ray system was able to measure the volume fraction in the recirculating cavity closure region, where the void fraction had strong spatial gradients. The non-unidirectional flow and strong gradients make the use of bubble point probes problematic. But, X-ray measurement is not affected by this, and also, the flow remains unperturbed. However, any X-ray data acquired with a system such as ours will often have non-negligible veiling glare. It should be taken into account when interpreting the data, and, as shown, it can be at least partially mitigated by deconvolution. The densitometry measurements revealed the spatial evolution of the time-averaged and fluctuating void fraction distribution in the cavity closure, and it was seen that even at $x/H = 21$ downstream of the backward-facing step, the void fraction distribution was evolving in the streamwise direction, and on average, the bubbles were migrating closer to the surface. It was also possible to observe the motion of the cavity closure as well as some of the largest individual bubbles in the wake region with the X-ray system. However, the spatial resolution of the X-ray system was not sufficient to resolve images of most individual bubbles, which were below 5 mm in diameter in the instantaneous frames.

Acknowledgments We acknowledge the assistance of Prof. Michael Flynn and Dr. Alexander Mychkovsky during the design of the X-ray densitometry system, and Mr. Christopher Haddad for his contribution in processing of the high-speed video images. The authors are grateful for the support of the Office of Naval Research under Grant N00014-10-1-0974 with Dr. L. P. Purtell, Program Manager.

References

Adams EW, Johnston JP (1988) Effects of the separating shear layer on the reattachment flow structure part 2: reattachment length and wall shear stress. Exp Fluids 6(7):493–499

Aeschlimann V, Barre S, Legoupil S (2011) X-ray attenuation measurements in a cavitating mixing layer for instantaneous two-dimensional void ratio determination. Phys Fluids 23:055101

Alles J, Mudde RF (2007) Beam hardening: analytical considerations of the effective attenuation coefficient of X-ray tomography. Med Phys 34(7):2882. doi:10.1118/1.2742501

Bushberg JT, Seibert JA, Leidholdt EM Jr, Boone JM (2001) The essential physics of medical imaging, 2nd edn. Lippincott Williams & Wilkins, Philadelphia

Cartelier A (1990) Optical probes for local void fraction measurements: characterization of performance. Rev Sci Instrum 61(2):874–886

Ceccio SL, George DL (1996) A review of electrical impedance techniques for the measurement of multiphase flows. J Fluids Eng 118(2):391–399

Cerveri P, Forlani C, Borghese NA, Ferrigno G (2002) Distortion correction for X-ray intensifiers: local unwarping polynomials and RBF neural networks. Am Assoc Phys Med 29(8):1759–1771

Cho J, Perlin M, Ceccio SL (2005) Measurement of near-wall stratified bubbly flows using electrical impedance. Meas Sci Technol 16(4):1021–1029

Clark NN, Turton R (1988) Chord length distributions related to bubble size distributions in multiphase flows. Int J Multiphase Flow 14(4):413–424

Coutier-Delgosha O, Stutz B, Vabre A, Legoupil S (2007) Analysis of cavitating flow structure by experimental and numerical investigations. J Fluid Mech 578:171–222

Elbing BR, Winkel ES, Lay KA, Ceccio SL, Dowling DR, Perlin M (2008) Bubble-induced skin-friction drag reduction and the abrupt transition to air-layer drag reduction. J Fluid Mech 612:201–236

Gabillet C, Colin C, Fabre J (2002) Experimental study of bubble injection in a turbulent boundary layer. Int J Multiphase Flow 28:553–578

George DL, Iyer CO, Ceccio SL (2000a) Measurement of the bubbly flow beneath partial attached cavities using electrical impedance probes. J Fluids Eng 122:151–155

George DL, Torczynski JR, Shollenberger KA, O'Hern TJ, Ceccio SL (2000b) Validation of electrical impedance tomography for measurement of material distribution in two-phase flows. Int J Multiphase Flow 26:549–581

Hassan W, Legoupil S, Chambellan D, Barre S (2008) Dynamic localization of vapor fraction in turbo pump inducers by X-ray tomography. IEEE Trans Nucl Sci 55(1):656–661

Heindel TJ (2011) A review of X-ray flow visualization with applications to multiphase flows. J Fluids Eng 133(7):074001. doi:10.1115/1.400436

Holder D (2005) Electrical impedance tomography: methods, history, and applications. IOP publishing, Bristol

Hubbell JH, Seltzer SM (2004) Tables of X-ray mass attenuation coefficients and mass energy-absorption coefficients (version 1.4). National Institute of Standards and Technology, Gaithersburg, MD. http://www.nist.gov/pml/data/xraycoef/index.cfm. Accessed 27 June 2011

Hubers JL, Striegel AC, Heindel TJ, Gray JN, Jensen TC (2005) X-ray computed tomography in large bubble columns. Chem Eng Sci 60:6124–6133

Johnson CB (1973) Point-spread functions, line-spread functions, and edge-response functions associated with MTFs of the form exp [-(w/w_r)^n]. Appl Opt 12(5):1031–1033

Julia JE, Harteveld WK, Mudde RF, Den Akker HEAV (2005) On the accuracy of the void fraction measurements using optical probes in bubbly flows. Rev Sci Instrum 76:35103

Mäkiharju SA (2012) The dynamics of ventilated partial cavities over a wide range of Reynolds numbers and quantitative 2D X-ray densitometry for multiphase flow. Ph.D. thesis, University of Michigan

Oweis G, Choi J, Ceccio SL (2004) Measurement of the dynamics and acoustic transients generated by laser induced cavitation bubbles. J Acoust Soc Am 115:1049–1058

Poludniowski G, Landry G, DeBlois F, Evans PM, Verhaegen F (2009) SpekCalc: a program to calculate photon spectra from tungsten anode X-ray tubes. Phys Med Biol 54(19):N433–N438. doi:10.1088/0031-9155/54/19/N01

Poludniowski G, Evans PM, Kavanagh A, Webb S (2011) Removal and effects of scatter-glare in cone-beam CT with an amorphous-silicon flat-panel detector. Phys Med Biol 56(6):1837–1851. doi:10.1088/0031-9155/56/6/019

Seibert JA, Boone JM (1988) Scatter removal by deconvolution. Med Phys 15(4):567

Seibert JA, Nalcioglu O, Roeck WW (1984) Characterization of the veiling glare PSF in X-ray image intensified fluoroscopy. Med Phys 11(2):172

Seibert JA, Nalcioglu O, Roeck W (1985) Removal of image intensifier veiling glare by mathematical deconvolution techniques. Med Phys 12(3):281

Smith EH (2006) PSF estimation by gradient descent fit to the ESF. In: Proceedings of SPIE, 6059 (January), 60590E–60590E-9. Spie. doi:10.1117/12.643071

Stutz B, Legoupil S (2003) X-ray measurements within unsteady cavitation. Exp Fluids 35:130–138

Thales electron devices (2006) Technical specification: X-ray image intensifier TH 9432 QX H686 VR13. Moiras, France

Van Der Welle R (1985) Void fraction, bubble velocity and bubble size in two-phase flow. Int J Multiphase Flow 11(3):317–345

York TJ (2001) Status of electrical tomography in industrial applications. J Electron Imaging 10:608